



## Green synthesis of mesoporous ZnFe<sub>2</sub>O<sub>4</sub>/C composite microspheres as superior anode materials for lithium-ion batteries

Lingmin Yao <sup>a,b</sup>, Xianhua Hou <sup>a,b,\*</sup>, Shejun Hu <sup>a,b</sup>, Jie Wang <sup>a,b</sup>, Min Li <sup>a,b</sup>, Chao Su <sup>c</sup>, Moses O. Tade <sup>c</sup>, Zongping Shao <sup>c</sup>, Xiang Liu <sup>d</sup>

<sup>a</sup> Laboratory of Quantum Engineering and Quantum Materials, School of Physics and Telecommunication Engineering, South China Normal University, Guangzhou 510006, China

<sup>b</sup> Engineering Research Center of Materials & Technology for Electrochemical Energy Storage (Ministry of Education), Guangzhou 510006, China

<sup>c</sup> Department of Chemical Engineering, Curtin University, Perth, WA 6158, Australia

<sup>d</sup> Institute of Advanced Materials, Nanjing University of Technology, Nanjing 210009, China



### HIGHLIGHTS

- Mesoporous ZnFe<sub>2</sub>O<sub>4</sub>/C microsphere composite was synthesized by hydrothermal method.
- The ZnFe<sub>2</sub>O<sub>4</sub>/C anode demonstrated high reversible capacity of 1100 mAh g<sup>-1</sup> after 100 cycles.
- The initial discharge/charge capacity was 1169 and 1551 mAh g<sup>-1</sup>, respectively.
- The high capacity retention of 97.6% was obtained for the ZnFe<sub>2</sub>O<sub>4</sub>/C anode after 100 cycles.

### ARTICLE INFO

#### Article history:

Received 4 November 2013

Received in revised form

9 January 2014

Accepted 15 February 2014

Available online 25 February 2014

#### Keywords:

Zinc ferrite

Mesoporous

Carbon network

Citric acid

### ABSTRACT

The commercialized LIBs employing graphite as anodes currently suffer a series of problems from the safety, theoretical capacity (372 mAh g<sup>-1</sup>) and rate capability. Herein, self-assembly mesoporous Zn ferrite (ZnFe<sub>2</sub>O<sub>4</sub>) microsphere embedded into carbon network has been synthesized by a facile method in the presence of citric acid. The Zn ferrites as an anode material with novel structure demonstrate superior electrochemical performance, with enhanced specific reversible capacity (~1100 mAh g<sup>-1</sup> at the specific current of 0.05 A g<sup>-1</sup> after 100 cycles), excellent rate capability (more than 500 mAh g<sup>-1</sup> even at the specific current of 1.1 A g<sup>-1</sup>) and good cycleability with little fading (~97.6% after 100 cycles). The excellent cycling performance is associated with the loose Zn ferrite microsphere with numerous mesopores embedded into the carbon network, which can accommodate the severe mechanism strains and provides good electrical contact and conductivity. The superior electrochemical performance may facilitate ZnFe<sub>2</sub>O<sub>4</sub> to be a promising alternative anode in lithium ion battery.

© 2014 Elsevier B.V. All rights reserved.

### 1. Introduction

Electrochemical energy storage (EES) has become an important technology which greatly benefits our modern convenience and helps to increase energy efficiency and reduce emissions during the utilization of fossil fuels and biofuels. As one of the most important types of EES systems, rechargeable lithium-ion batteries (LIBs) have demonstrated a great success in personal electronic devices. With the increasing concerns about environmental protection and ever-

diminishing resources of fossil fuels, the potential large-scale applications of LIBs as power sources of electric vehicles and energy storage system for smart grids have also received considerable attentions [1–4].

The state-of-the-art LIBs employ graphite as the anode material, which is characterized by a relatively low theoretical capacity of 372 mAh g<sup>-1</sup> and near zero potential for lithium intercalation reaction. Additionally, such LIBs have the drawbacks of poor power performance related to the release of the solvation shell upon lithium ion intercalation. To realize large-scale applications of LIBs, it is critical to develop alternative anode materials that have much improved capacity, rate capability and cycling stability.

There are mainly three types of anode materials for LIBs based on the charge storage mechanism: (a) the intercalation material

\* Corresponding author. Laboratory of Quantum Engineering and Quantum Materials, School of Physics and Telecommunication Engineering, South China Normal University, Guangzhou 510006, China. Tel.: +86 02039318011.

E-mail addresses: [houxh@scnu.edu.cn](mailto:houxh@scnu.edu.cn) (X. Hou), [\(Z. Shao\).](mailto:zongping.shao@curtin.edu.au)

such as graphite which store the charge by intercalating the lithium-ion into their planar structure, and insertion materials such as  $\text{Li}_4\text{Ti}_5\text{O}_{12}$  spinel oxides and  $\text{TiO}_2$  anatase [5–7]; (b) the lithium-alloying materials, such as Sn and Si, which store charge by forming lithium-metal alloy [8–10]; and (c) conversion materials, such as transition metal oxides like  $\text{MnO}$  and  $\text{Fe}_3\text{O}_4$ , which store charge via the conversion reaction ( $\text{MO}_x + 2x\text{Li}^+ + 2x\text{e}^- \leftrightarrow \text{M} + x\text{Li}_2\text{O}$ ) [11–13]. The anode materials based on the conversion reaction mechanism are of particular interest for their large number of choices, high theoretical capacity and improved discharge potential as compared to graphite for avoiding lithium dendrite formation under fast discharge rate. Thus, currently there are considerable research activities in the development of novel anode materials for LIBs based on the conversion mechanism [14–18].

Among the various transition oxide materials, iron-based binary and ternary oxides have been mostly investigated for their high theoretical capacity, rich resource, and environmental benignity [19–23]. As a composite oxide with a spinel lattice structure,  $\text{ZnFe}_2\text{O}_4$  is of particular interest as an anode material for LIBs with theoretical capacity as large as  $1000 \text{ mAh g}^{-1}$  [24–27]. Unlike most types of oxides, the lithium insertion into  $\text{ZnFe}_2\text{O}_4$  electrode involves both the mechanisms of conversion and alloying reactions. After the conversion of  $\text{ZnFe}_2\text{O}_4$  by the reaction with lithium ions with the formation of Zn, Fe and  $\text{Li}_2\text{O}$ , the Zn product could further react with lithium to form  $\text{ZnLi}_x$  alloy, thus contributing additional capacity.

The main challenges associated with  $\text{ZnFe}_2\text{O}_4$  as electrodes of LIBs are large irreversible capacity at first discharge–charge cycle, poor power capability, and fast decay in capacity with cycle time, mainly resulted from poor electrical conductivity and large volumetric change associated with the conversion reaction. During the past, materials modification (doping) and morphological optimization (size control, specific particulate morphology and pore structure development) are the main strategies to improve the electrochemical performance in LIBs [28–32]. Reducing the size of electrode materials to nanometer range or introducing mesopores into the electrode materials could improve the rate capability by reducing the lithium-diffusion distance and increase the capacity by maximizing the electro-active zones of electrodes [33,34]. On the other hand, the introduction of a buffer medium to accommodate the volume expansion of electrode materials during the electrochemical reaction process is also an effective way to improve the cycling stability [35,36]. Among the various materials, carbon is most attractive because of its low weight, high conductivity and rich recourse. During the past several years, several attempts were also performed to improve the electrochemical performance of  $\text{ZnFe}_2\text{O}_4$  in LIBs, such as synthesis of hollow microspheres [37], surface coating with carbon [32], decreasing of particle size to the nanometer range through advanced synthesis [39]. Among the various synthetic methods, hydrothermal and solvothermal processes have turned out to be highly versatile in the synthesis of  $\text{ZnFe}_2\text{O}_4$  of various morphologies with favorable electrode performance [26,32]. For example, recently, Ju et al. reported the hydrothermal synthesis of  $\text{ZnFe}_2\text{O}_4$  octahedrons using high toxic  $\text{N}_2\text{H}_4 \cdot \text{H}_2\text{O}$ , achieving a capacity of  $910 \text{ mAh g}^{-1}$  after 80 charge–discharge cycles at  $0.06 \text{ A g}^{-1}$  specific current [26]. Although good performance has been reported, the complicated fabrication process still hinders the large-scale production of  $\text{ZnFe}_2\text{O}_4$  for practical LIBs with economic attractiveness.

Herein, mesoporous  $\text{ZnFe}_2\text{O}_4/\text{C}$  composite for LIBs by a facile hydrothermal reaction route with citric acid as an inexpensive, non-toxic reducing agent and stabilizer in combination with a simple calcinations step under inert atmosphere, was reported. The specific composites, consisted of  $\text{ZnFe}_2\text{O}_4$  nanoparticles coating with a thin layer of pyrolyzed conductive carbon, were self-

assembled into mesoporous microspheres. By applying such material as an anode in LIBs, a capacity as high as  $1100 \text{ mAh g}^{-1}$  was obtained after charge–discharge cycling at  $0.05 \text{ A g}^{-1}$  specific current for 100 times, achieving a capacity retention of 97.6% as compared with that at 10th cycle. The electrode also showed excellent rate capability, reaching a capacity of  $560 \text{ mAh g}^{-1}$  even at  $1.1 \text{ A g}^{-1}$  specific current, which is among the best results about  $\text{ZnFe}_2\text{O}_4$ -based electrodes available in literature. It thus makes  $\text{ZnFe}_2\text{O}_4$  a highly promising alternative anode to graphite for LIBs with great practical application potentials.

## 2. Experimental

### 2.1. Preparation and characterization of $\text{ZnFe}_2\text{O}_4/\text{C}$ composites

All chemicals (received from Sinopharm Chemical Reagent Co., Ltd) used in the experiment were of analytic grade used as received without any further purification. In a typical synthesis, 8 mmol zinc chloride ( $\text{ZnCl}_2$ ), 16 mmol hydrated iron chloride ( $\text{FeCl}_3 \cdot 6\text{H}_2\text{O}$ ) and 45 mmol ammonium acetate ( $\text{NH}_4\text{Ac}$ ) were dissolved in a mixture of ethylene glycol and deionized water with constant stirring for 1 h. Then 2.6 mmol citric acid was introduced into the mixed solution. Subsequently, the homogeneous solution was transferred into a Teflon-lined stainless steel autoclave (150 ml in volume) and treated hydrothermally at  $200^\circ\text{C}$  for 24 h to get the precipitate of  $\text{ZnFe}_2\text{O}_4$  particles. Finally, the obtained  $\text{ZnFe}_2\text{O}_4$  particles were sintered at  $600^\circ\text{C}$  for 5 h under a flowing  $\text{N}_2$  atmosphere to form mesoporous  $\text{ZnFe}_2\text{O}_4/\text{C}$  composite microspheres. For comparison, carbon-free  $\text{ZnFe}_2\text{O}_4$  particles without adding citric acid were also prepared by the same way as described above.

The crystal structure and morphology of the as-prepared  $\text{ZnFe}_2\text{O}_4/\text{C}$  composite were characterized by X-ray diffraction (XRD, PANalytical X'Pert PRO, Cu  $\text{K}\alpha$  radiation,  $\lambda = 1.5406 \text{ nm}$ ), micro-Raman spectroscope (Jobin Yvon LabRam HR800), scanning electron microscopy (SEM, ZEISS ULTRA 55) and transmission electron microscopy (TEM, JEM-2100HR) with Energy Dispersive Spectrometer (EDS). The element contents were examined by energy-dispersive X-ray spectroscopy (EDS). The porous nature of the samples was investigated using physical adsorption of nitrogen at liquid-nitrogen temperature on an automatic volumetric sorption analyzer (NO-VA3200e, Quantachrome).

The specific surface area was determined according to the Brunauer–Emmett–Teller (BET) method in the relative pressure range of 0.05–0.2. Pore size distribution (PSD) curves were derived from the Barrett–Joyner–Halenda (BJH) method using the adsorption branches. The pore-size distribution was estimated from the maximum positions of the BJH PSD curves. The TGA was carried out by heating the dry powder samples at a rate of  $10^\circ\text{C min}^{-1}$  in NEZSCH STA 409.

### 2.2. Electrochemical performance

The electrochemical performance of  $\text{ZnFe}_2\text{O}_4/\text{C}$  composite and  $\text{ZnFe}_2\text{O}_4$  were evaluated by using coin-type half-cells (CR2530) assembled in an argon-filled glove box. For comparison, all working electrodes for electrochemical tests were composed of 70 wt.% active material, 15 wt.% Super P as conducting agent and 15 wt.% PVDF as binder on the copper foil with a wet film thickness of 150  $\mu\text{m}$ . PVDF, Super P, and the copper foil have been received from BTR battery Materials Co., Ltd. The electrolyte was  $1.0 \text{ M LiPF}_6$  in a mixture of ethylene carbonate (EC), diethyl carbonate (DEC) and ethyl methyl carbonate (EMC) (1:1:1 by volume, provided by Cheil Industries Inc., South Korea). The separator was made of a Celgard 2400 film. High purity Li (Aldrich) was used to prepare counter and reference electrode.

The cycling performance of the cells were evaluated in a constant current (CC) mode at a specific current of  $0.05 \text{ A g}^{-1}$  in the voltage range of  $0.001\text{--}3.0 \text{ V}$  (CT2001A, LAND). In this report, the lithiation was expressed as discharging, whereas the delithiation as charging. Cyclic voltammetry (CV) measurements were performed using electrochemical workstation (1470E, Solartron Analytical) at a scan rate of  $0.1 \text{ mV s}^{-1}$  in the range of  $0.0\text{--}3.0 \text{ V}$ . Impedance measurements were acquired in the frequency ranging from  $0.01 \text{ mHz}$  to  $100 \text{ kHz}$ . All the potentials were given vs.  $\text{Li}/\text{Li}^+$  redox couple. The cells were performed at the specific current of  $0.05 \text{ A g}^{-1}$  to get the complete and homogeneous solid electrolyte interface (SEI) in the first 3 cycles.

### 3. Results and discussion

The precipitator from the hydrothermal process with the presence of citric acid during the synthesis was in the color of light black while it was in yellowish-brown color for the solid precursor without citric acid. After the further calcination of  $\text{ZnFe}_2\text{O}_4/\text{C}$  solid precursor under  $\text{N}_2$  atmosphere, a powder with dark black color was obtained. It strongly suggested carbon was successfully formed in the product, likely produced from the pyrolysis of citric acid; as a comparison, pure  $\text{ZnFe}_2\text{O}_4$  composite oxide was typically in bright yellow color. Fig. 1 illustrates the XRD pattern of the product after the heat treatment of precipitate from the hydrothermal synthesis at  $600^\circ\text{C}$ . The diffraction peaks matched pretty well with those of a spinel-type  $\text{ZnFe}_2\text{O}_4$  (JCPDS Card No. 022-1012), suggesting the successful formation of  $\text{ZnFe}_2\text{O}_4$  phase. It is suggested that reductive CO can be produced in the carbonization process under a higher temperature according to Mueller et al. [25]. However, it should be noted that additional peaks connected with  $\text{ZnO}$  and  $\text{FeO}$  due to CO could not be detected for the sample. It implies the reducing products (CO,  $\text{H}_2$  and solid carbon) from the thermal decomposition of citric acid did not cause the deep reduction of iron ions in the sample. The high peak intensity indicated good crystallinity of the  $\text{ZnFe}_2\text{O}_4$  phase. The diffraction patterns were further conducted by Rietveld refinement based on a spinel structure with  $\text{Fd}-3\text{m}$  space group. The narrow peak width indicated a good crystallinity. The lattice parameter  $a$  was turned out to be  $0.8437 \text{ nm}$ , agreeing pretty well with  $0.8441 \text{ nm}$  of standard  $\text{ZnFe}_2\text{O}_4$  (JCPDS Card No. 022-1012). Based on the half width of the (110) diffraction peak, the mean crystalline size was approximately

$16.8 \text{ nm}$ , calculated using the Scherrer equation, suggesting nano-size nature of the  $\text{ZnFe}_2\text{O}_4$  phase.

No any diffraction peak assignable to crystalline phase of carbon was detected from the XRD patterns, suggesting the carbon phase was likely in amorphous structure. The product was then further subjected for characterization by the Raman spectroscopy. As shown in Fig. 2, two adsorption peaks at wave numbers of  $1356.88 \text{ cm}^{-1}$  and  $1594.23 \text{ cm}^{-1}$  were observed, which can be assigned to the D band and G band of carbon. D band usually results from carbon with lattice defects, disordered carbon at the edge and low-symmetry carbon, while the G band results from the stretch vibration of  $\text{sp}^2$  hybrid carbon in carboatomic rings or long chain carbon [40]. The  $I_D/I_G$  ratio is an indication of the graphitization degree of the carbon, which was turned out to be around 2.8 for the carbon in current sample; as a comparison, the value for graphite was reported to be typically less than 1.0 [41]. It strongly suggests that the carbon was mainly in amorphous state in the as-prepared  $\text{ZnFe}_2\text{O}_4/\text{C}$  composite, agreeing well with the XRD results. It may be explained by the low calcinations temperature. The amount of carbon inside the sample was then determined by TGA, and it was turned out to be around 6.4 wt.%.

Morphology of the precursor for  $\text{ZnFe}_2\text{O}_4/\text{C}$  composite directly from hydrothermal synthesis and the product after further calcination at  $600^\circ\text{C}$  were first characterized by SEM. For the solid precursor, semi-spherical particles in the size of around  $1 \mu\text{m}$  were observed, which were however glue together tightly (Fig. 3a). Interestingly, after the calcination at  $600^\circ\text{C}$ , as shown in Fig. 3b, the particles in the size of  $1\text{--}1.5 \mu\text{m}$  became well separated from each other and their spherical shape became more perfect. Fig. 3c presents a magnified image of selected particles. It clearly showed that the spheres were actually secondary particles constructed from nanosized particles. An examination of some particular microspheres by EDS, with the profile shown in Fig. 3d, demonstrated that the particles were mainly composed of Zn, Fe and O elements (Fig. 3e), matching well with the composition of target material of  $\text{ZnFe}_2\text{O}_4$ . Strong carbon peak was also detected, suggesting the presence of carbon, as expected. To further observe the microstructure inside the microspheres, some of them were cut by a blade. As shown in Fig. 3f, it was a typical SEM image of some cut microspheres. It demonstrated that the secondary particles were porous and homogeneous in composition throughout the entire particle. Previously we synthesized  $\text{ZnFe}_2\text{O}_4$  micrometer-sized

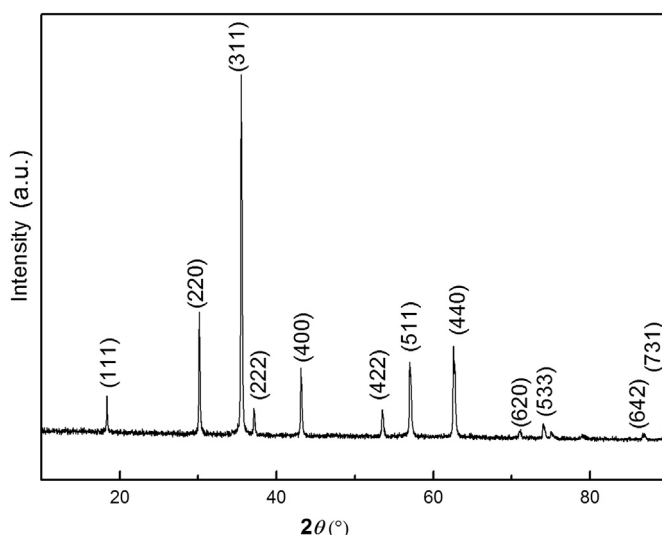


Fig. 1. XRD pattern of  $\text{ZnFe}_2\text{O}_4/\text{C}$  composites.

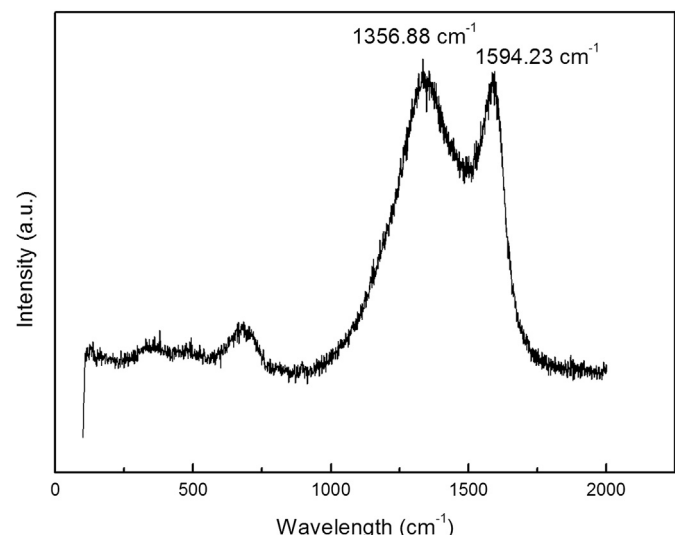
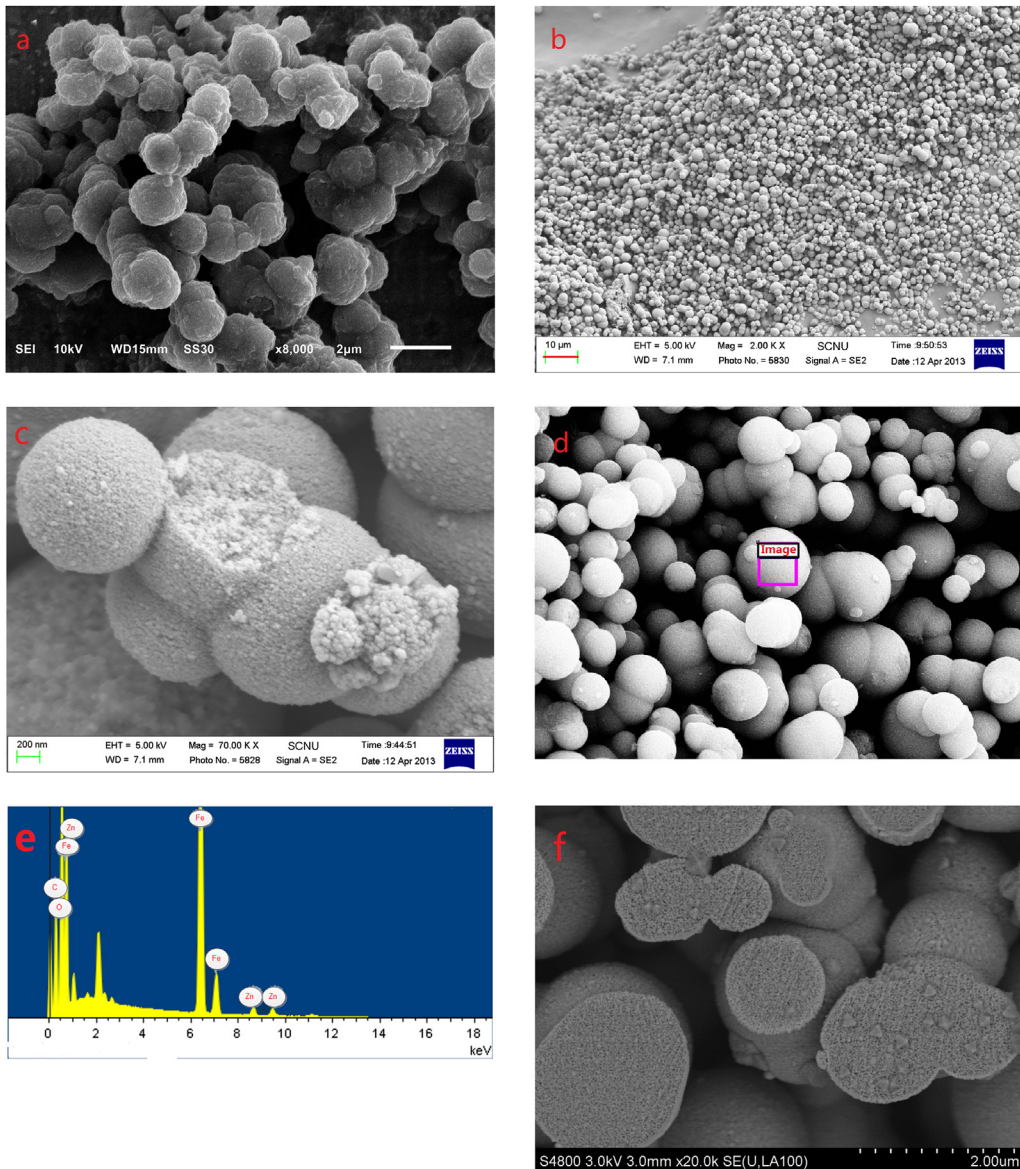


Fig. 2. Raman spectroscopic of  $\text{ZnFe}_2\text{O}_4/\text{C}$  composites.



**Fig. 3.** (a) Representative SEM images of  $\text{ZnFe}_2\text{O}_4/\text{C}$  composites before calcination and (b) after calcination at  $600\text{ }^\circ\text{C}$ ; (c) SEM image of partial enlarged detail; (d and e) EDS images of the selective area; (f) SEM image of a cross-section of  $\text{ZnFe}_2\text{O}_4/\text{C}$  microspheres.

particles with a hollow sphere morphological structure by a similar hydrothermal process [31]. It suggests the slight change in process parameters of hydrothermal synthesis could induce a big effect on the morphology of the final products.

To get more information about microstructure of the microspheres, they were further subjected for TEM observation with the typical image shown in Fig. 4a. It was almost in perfect round shape with a diameter of 800 nm. The contrast between the dark and the light colors dispersed homogeneously throughout the sphere, implying its porous structure. A larger magnification of part of the sphere was shown in Fig. 4b, which clearly demonstrated that the microsphere was built from nanoparticles in the size of 10–50 nm, agreeing well with the crystalline size of around 16.8 nm as calculated from half-width of diffraction peak in XRD pattern using Scherrer equation. Homogeneous distribution of pores inside the microspheres was clearly demonstrated, and such pores in the size of nanometer range were formed from the void space among aggregated nanoparticles. A HR-TEM image of particular nano-

particle was shown in Fig. 4c. Clear fringes with lattice spacings of 0.489 and 0.255 nm were observed, which matched pretty well with the distances of {111} and {311} diffraction planes for the cubic spinel  $\text{ZnFe}_2\text{O}_4$  (JCPDS Card No. 022-1012), respectively. It further confirmed that the spinel phase  $\text{ZnFe}_2\text{O}_4$  was formed in the as-synthesized microsphere powders. Near the surface of  $\text{ZnFe}_2\text{O}_4$  particles, an amorphous layer was observed, which was assigned to the amorphous carbon, suggesting the presence of solid carbon.

The microstructural feature of  $\text{ZnFe}_2\text{O}_4/\text{C}$  microspheres was further investigated by nitrogen isothermal adsorption with the corresponding isotherm shown in Fig. 5a. The nitrogen adsorption–desorption isotherm belongs to type IV category according to international union of pure and applied chemistry classification, suggesting the presence of mesopores. The distinct hysteresis loop indicated that those  $\text{ZnFe}_2\text{O}_4$  microspheres possessed cylindrical mesopores with open ends. The pore-size distribution spectrum as shown in Fig. 5b, obtained by the Barrett–Joyner–Halenda method, clearly illustrated the presence of mesopores, which were mainly

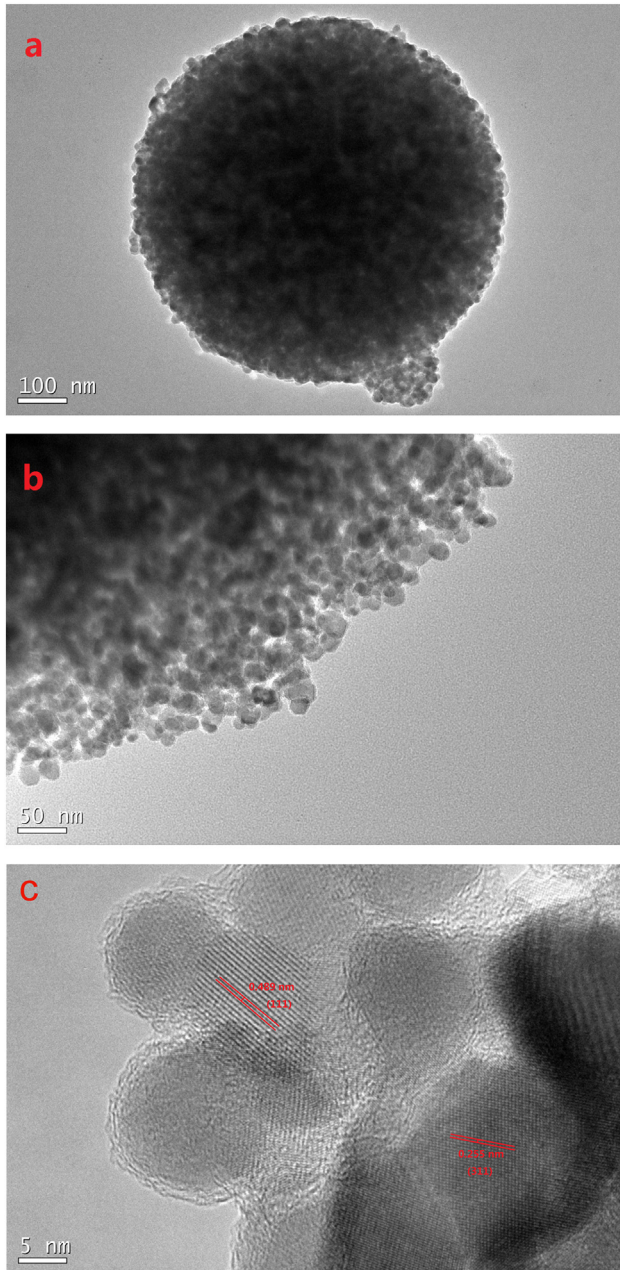


**Fig. 4.** (a) TEM images of the single  $\text{ZnFe}_2\text{O}_4/\text{C}$  microsphere; (b) the enlarged edge detail of the microsphere; (c) lattice fringes of the  $\text{ZnFe}_2\text{O}_4/\text{C}$  microsphere.

located in the narrow range of 5–20 nm, and peaked at 11 nm. In connection with the TEM image as shown in Fig. 4, such pores were formed mainly from the stacking of nanoparticles. The Brunauer–Emmett–Teller (BET) specific surface area of the microspheres was found to have a medium value of around  $46.8 \text{ m}^2 \text{ g}^{-1}$ . Such areas may come from the outer surface of  $\text{ZnFe}_2\text{O}_4$  nanoparticles as well as the amorphous carbon. By considering the low carbon weight (6.4 wt.%), the surface area was mainly contributed from the outer surface of nanoparticles. It should be mentioned that too high surface area could lead to more serious side reactions between electrode and liquid electrolyte in LIBs, inducing poor coulombic efficiency in the first charge–discharge cycle.

For comparison, we also prepared  $\text{ZnFe}_2\text{O}_4$  by the similar hydrothermal process, keeping all the other parameters the same to

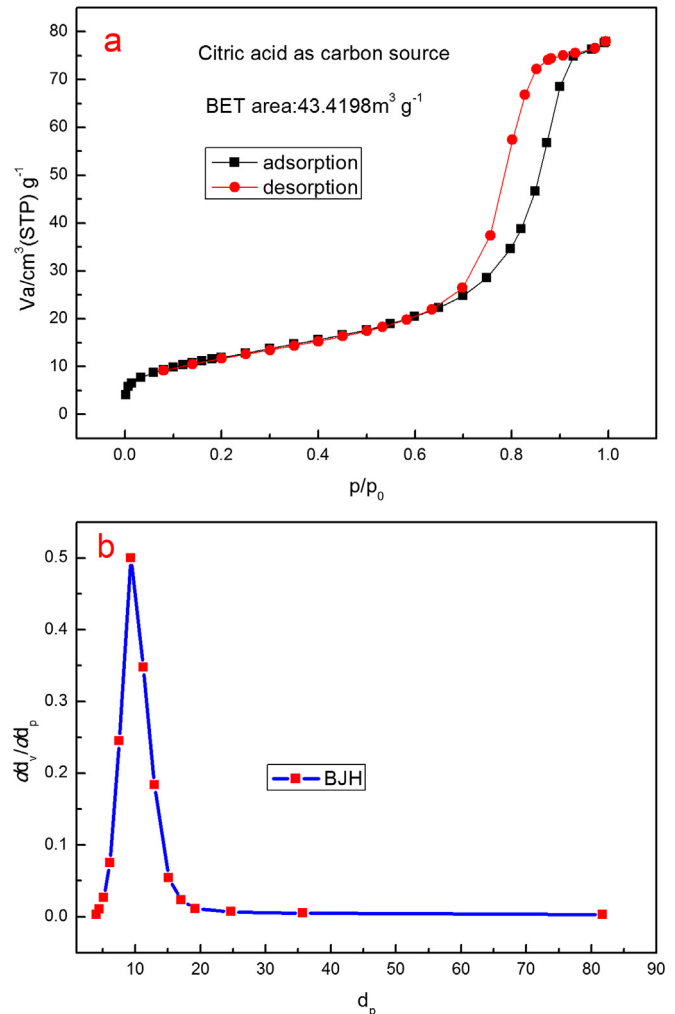


**Fig. 5.** (a) Nitrogen adsorption/desorption isotherms of the  $\text{ZnFe}_2\text{O}_4/\text{C}$  composite; (b) The pore-size distribution of the  $\text{ZnFe}_2\text{O}_4/\text{C}$  composites analyzed by Barrett–Joyner–Halenda (BJH) method.

the synthesis of  $\text{ZnFe}_2\text{O}_4/\text{C}$  particles, while the only difference was that no citric acid was used during the synthesis. Single phase  $\text{ZnFe}_2\text{O}_4$  was formed after the calcinations of the solid precursor at  $600^\circ\text{C}$  in inert atmosphere, suggesting the citric acid did not have an impact on the formation of  $\text{ZnFe}_2\text{O}_4$  phase. The particles were also in spheric morphological shape as shown in Fig. 6. However, based on the  $\text{N}_2$  adsorption/desorption isotherm as shown in Fig. 7a, a much smaller BET specific surface area of  $16.1 \text{ m}^2 \text{ g}^{-1}$   $\text{ZnFe}_2\text{O}_4$  was calculated, which was only about one third that of  $\text{ZnFe}_2\text{O}_4/\text{C}$  composite, suggesting the more sintered nature of carbon-free  $\text{ZnFe}_2\text{O}_4$ . The pore size distribution in Fig. 7b demonstrated that  $\text{ZnFe}_2\text{O}_4$  had much smaller pore volume ( $0.11 \text{ ml g}^{-1}$  as a comparison of  $0.13 \text{ ml g}^{-1}$  for  $\text{ZnFe}_2\text{O}_4/\text{C}$ ) and much larger pore size. Typically, the increase in particle size due to sintering would lead to porous structure since the pores were formed from the void space of the stacking of the particles. It suggests the carbon formed from the pyrolysis of citric acid for the synthesis of  $\text{ZnFe}_2\text{O}_4/\text{C}$  acted as a diffusion block to effectively suppress the sintering of  $\text{ZnFe}_2\text{O}_4$  nanoparticles during the calcination.

In combination with the results from others, a mechanism for the formation of the specific mesoporous microspheres via the hydrothermal process with the presence of citric acid was proposed and schematically shown in Fig. 8. Firstly,

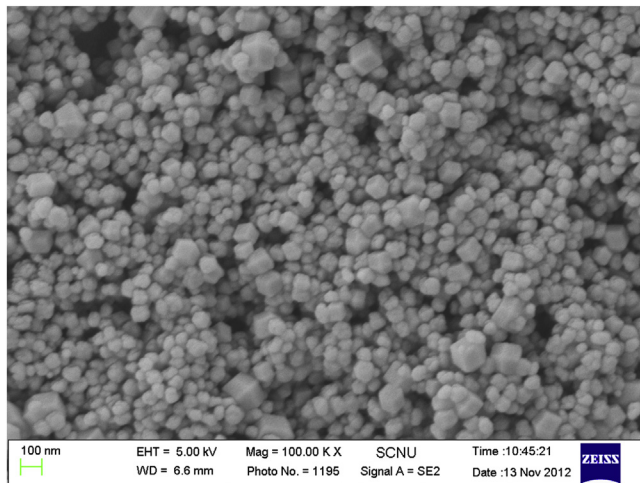


**Fig. 6.** Representative SEM images of pure  $\text{ZnFe}_2\text{O}_4$  composites.

primary  $\text{ZnFe}_2\text{O}_4$  nucleations under the hydrothermal reaction ( $\text{Zn}^{2+} + \text{Fe}^{3+} + 4\text{H}_2\text{O} = \text{ZnFe}_2\text{O}_4 + 8\text{H}^+$ ) condition was happened; then the ethylene glycol and citric acid were absorbed onto the surface of the primary nanosized  $\text{ZnFe}_2\text{O}_4$  and acted as structuring-direction and binder agent to influence the aggregation of the

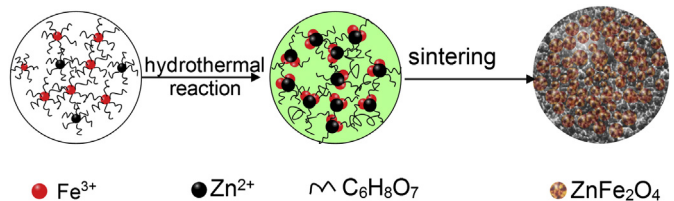


**Fig. 8.** The synthetic illustration of the mesoporous  $\text{ZnFe}_2\text{O}_4/\text{C}$  as an anode in lithium ion battery.

nano-particles, leading them to assemble by themselves to form microspheres [42]. The sphere size was determined by several factors including pH, the concentration of solution and reaction time. After the further calcinations at  $600^\circ\text{C}$ , thermal decomposition of the citric acid was happened to form amorphous carbon, coating on the surface of the nanoparticles in the microspheres, which acted as a binder for the nanoparticles to increase the mechanical strength during the later electrochemical charge–discharge cycling. The carbon also effectively suppressed the sintering of nanoparticles, allowing the creation of rich mesopores inside the microspheres.

The spherical shape of the  $\text{ZnFe}_2\text{O}_4$  particles allows a high particulate fluidity, thus making it easy to achieve highly homogeneous electrode film and to obtain high pack density of the electrode material. On the other hand, the rich mesopores presented inside the microspheres may facilitate the  $\text{Li}^+$  diffusion between the electrolyte and active sites with less resistance. More importantly, the interstitial space could effectively accommodate the mechanical strains caused by the volume expansion during the charge–discharge process. Additionally, the conductive carbon coating is beneficial to improve the intrinsic electrical conductivity. All above factors imply that the  $\text{ZnFe}_2\text{O}_4/\text{C}$  composite may exhibit improved electrochemical performance in terms of specific capacity, rate capability and cycling stability.

### 3.1. Electrochemical performance

To determine the electrochemical performance of the as-prepared  $\text{ZnFe}_2\text{O}_4/\text{C}$  mesoporous microspheres, half cell using  $\text{ZnFe}_2\text{O}_4/\text{C}$  composite as working electrode and lithium metal as counter and reference electrode was built. The electrode performance was first evaluated by galvanostatic charge–discharge test. As shown in Fig. 9a, for the  $\text{ZnFe}_2\text{O}_4/\text{C}$  electrodes, the charge capacities reached 1169, 1173, 1162 and 1187  $\text{mAh g}^{-1}$ , respectively at the 1st, 2nd, 50th and 100th cycles, at a specific current of  $0.05 \text{ A g}^{-1}$ . The coulombic efficiency for the first cycle reached about 75.5%, and the main irreversible capacity was likely contributed from the SEI formation. Anyway, such reversible capacity was already among the highest in literature for  $\text{ZnFe}_2\text{O}_4$ -based electrodes [32,37–39], suggesting the good reversibility of the electrode reaction, likely related to the carbon coating which protected the electrode materials from direct exposure to liquid electrolyte. For all subsequent cycles, the coulombic efficiency maintained at >97%. The reversible capacity for current  $\text{ZnFe}_2\text{O}_4/\text{C}$  electrode even slightly exceeded its theoretical capacity, it was likely the carbon conductive additive may also contribute partial capacity due to low end of discharge potential (0.001 V). The shape of galvanostatic charge–discharge curves observed in this study was consistent with that of previous report for  $\text{ZnFe}_2\text{O}_4$  anodes [24]. In the first discharge process, the voltage exhibited a drastic drop until the specific capacity reached about  $45 \text{ mAh g}^{-1}$  forming with  $\text{Li}_{0.4}\text{ZnFe}_2\text{O}_4$ . Then a short voltage plateau is shown up between 1.0 V and 0.8 V, and the specific capacity reached about

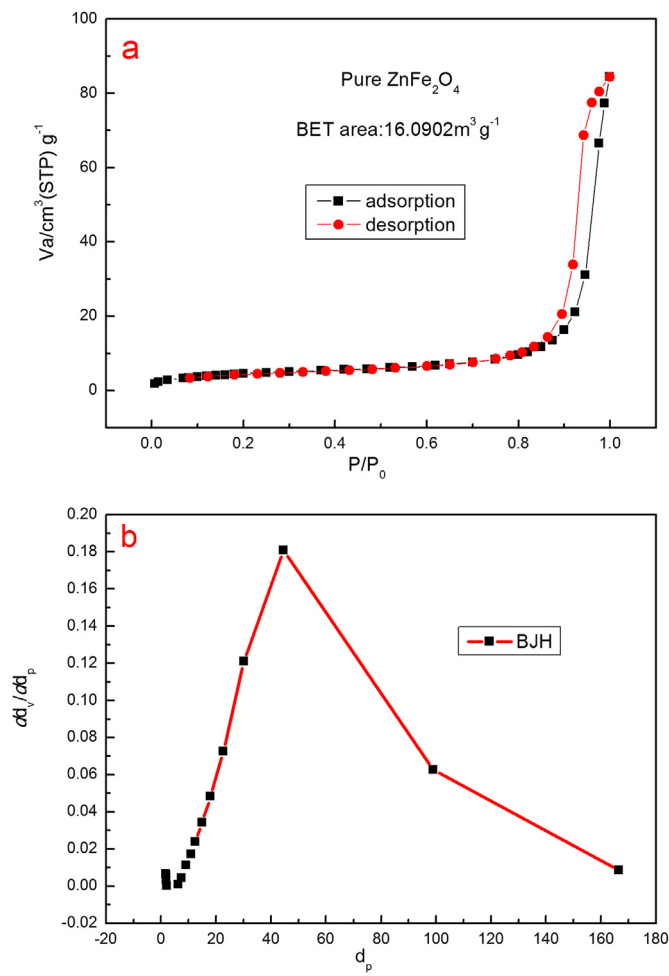


**Fig. 7.** (a) Nitrogen adsorption/desorption isotherms, and (b) the pore-size distribution, of the pure  $\text{ZnFe}_2\text{O}_4$  composites analyzed by BJH method.

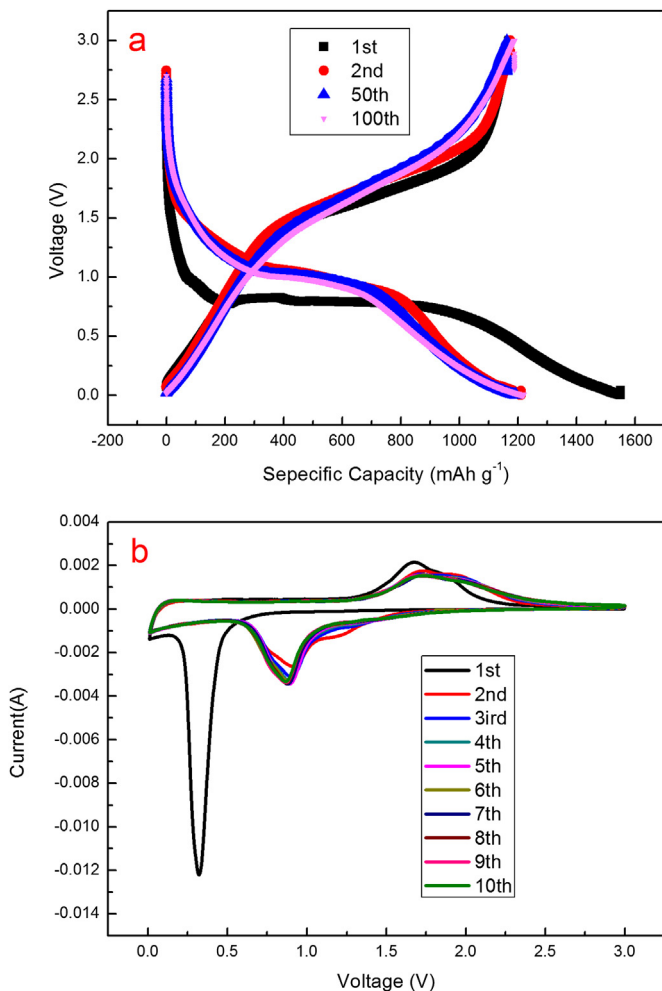


**Fig. 9.** (a) The voltage–capacity profiles for the 1st, 2nd, 50th and 100th cycles at the specific current of  $0.05 \text{ A g}^{-1}$ ; and (b) cyclic voltammetry curves at a rate  $0.1 \text{ mV s}^{-1}$  of the as-obtained  $\text{ZnFe}_2\text{O}_4/\text{C}$  electrode.

$220 \text{ mAh g}^{-1}$  ( $\sim 2 \text{ mol}$  of Li insertion). A more obvious long voltage plateau at  $0.8 \text{ V}$  is obtained, and the specific capacity reaches about  $900 \text{ mAh g}^{-1}$  (a whole  $\sim 8 \text{ mol}$  of  $\text{Li}^+$  is consumed), corresponding to the reduction of  $\text{Fe}^{3+}$ ,  $\text{Fe}^{2+}$  and  $\text{Zn}^{2+}$  to  $\text{Fe}^0$  and  $\text{Zn}^0$  as well as the formation of amorphous  $\text{Li}_2\text{O}$ . As the voltage approached gradually to  $0.01 \text{ V}$ , the formation of Li–Zn alloy and SEI might also be appeared. However, shorter and higher profile plateaus stabilized at  $0.95 \text{ V}$  after the initial cycle, which accompanied by crystal structure destruction. As to the first charge profile, a short steady increasing voltage plateau at  $1.5$ – $1.8 \text{ V}$  was observed. From the second discharge–charge cycle on, the voltage–capacity profiles almost kept the same for the remaining cycles, indicating the good capacity retention of the  $\text{ZnFe}_2\text{O}_4/\text{C}$  anode material.

To further clarify the thermodynamics of the lithiation–delithiation processes in  $\text{ZnFe}_2\text{O}_4/\text{C}$  electrode, the CVs have been recorded at a scan rate of  $0.1 \text{ mV s}^{-1}$  in the potential range from  $3.0$  to  $0.0 \text{ V}$ . Fig. 9b illustrated the initial 10 cycles of the CV curves, which matched well in shape with that of previous report for pure  $\text{ZnFe}_2\text{O}_4$  electrode [26]. In the initial cycle, the sharp cathodic peak located at  $0.3 \text{ V}$  was corresponding to the reduction of  $\text{Fe}^{3+}$ ,  $\text{Fe}^{2+}$  and  $\text{Zn}^{2+}$  to  $\text{Fe}^0$  and  $\text{Zn}^0$ . However, it disappeared in the following cycles, and shifted to  $0.95 \text{ V}$ , agreeing well with the discharge potential plateau as shown in Fig. 5. The large decrease in integrated area between the first cycle and the following cycles was consistent

with the relatively low initial coulombic efficiency of 75.5%, indicating the capacity loss caused by electrolyte decomposition, electrode pulverization and SEI film formation. While the initial anodic peaks located at  $1.5$  and  $1.7 \text{ V}$ , afterward shifting right to  $1.6$  and  $1.8 \text{ V}$ , respectively, were associated with the Li insertion reactions with the reversible oxidation of  $\text{Fe}^0$  and  $\text{Zn}^0$  to  $\text{Fe}^{3+}$ ,  $\text{Fe}^{2+}$  and  $\text{Zn}^{2+}$ . It was noted that all the characteristic peaks and the integrated area almost maintained the same after the first cycle, further revealing the excellent capacity retention of  $\text{ZnFe}_2\text{O}_4/\text{C}$  mesopores electrodes.

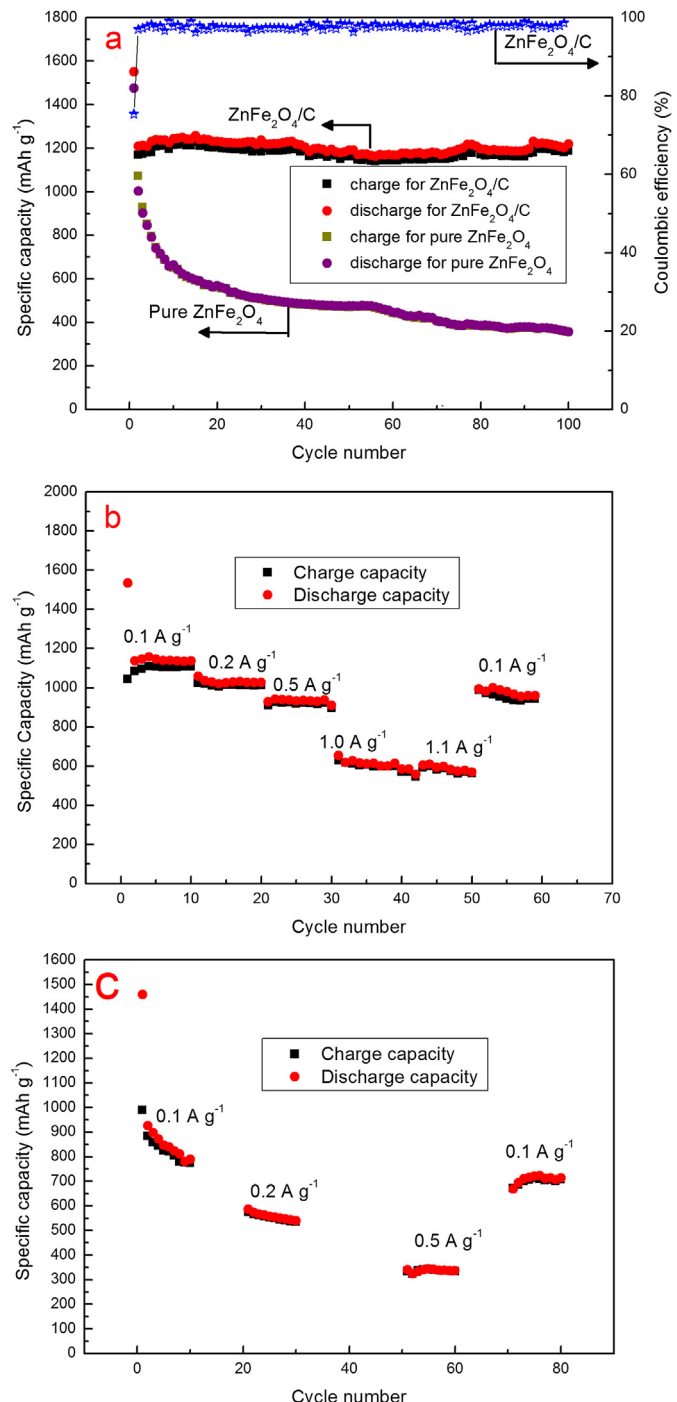


**Fig. 10.** (a) Cycle performance of pure  $\text{ZnFe}_2\text{O}_4$  and  $\text{ZnFe}_2\text{O}_4/\text{C}$  electrodes at the specific current of  $0.05 \text{ A g}^{-1}$ ; (b) rate capability of  $\text{ZnFe}_2\text{O}_4/\text{C}$  electrodes and (c) pure  $\text{ZnFe}_2\text{O}_4$  without citric acid.

**Fig. 10a** illustrated the cycling performance of pure ZnFe<sub>2</sub>O<sub>4</sub> and ZnFe<sub>2</sub>O<sub>4</sub>/C electrodes prepared from the similar hydrothermal processes. As for the pure ZnFe<sub>2</sub>O<sub>4</sub>, the initial charge and discharge capacities were 1475 and 1072 mAh g<sup>-1</sup>, respectively, with a coulombic efficiency of 72.6%. Unfortunately, the capacity decayed rapidly to 600 mAh g<sup>-1</sup> in the subsequent 10 cycles, it was still decreased under further cycling to only 350 mAh g<sup>-1</sup> at 100th cycle. Such a large capacity loss for pure ZnFe<sub>2</sub>O<sub>4</sub> electrode was associated with its low intrinsic electrical conductivity and large volume expansion and potential aggregation of nanoparticles during charge–discharge process. For comparison, the ZnFe<sub>2</sub>O<sub>4</sub>/C electrode demonstrated much improved electrochemical performance. As can be seen from the **Fig. 10a**, the initial charge and discharge capacities approached 1169 and 1551 mAh g<sup>-1</sup>, respectively, at a specific current 0.05 A g<sup>-1</sup>. Although the coulombic efficiency for the first cycle was 75.5%, which was only slightly higher than that of pristine ZnFe<sub>2</sub>O<sub>4</sub> prepared by a similar process, it quickly increased to near 97% at the second cycle and then maintained such a high value in the following cycles, indicating high efficiency and reversibility of the lithium insertion/extraction in ZnFe<sub>2</sub>O<sub>4</sub>/C composite. A reversible specific capacity as high as ~1150 mAh g<sup>-1</sup> was still achieved after charge–discharge cycle at 0.05 A g<sup>-1</sup> for 100 cycles, which was about 90% that of the 10th cycle, demonstrating the outstanding cycling stability of ZnFe<sub>2</sub>O<sub>4</sub>/C electrode. From the 2nd circle on, the charge capacity increased slightly to reach 1221 mAh g<sup>-1</sup> at the 13th cycle. Such an improvement can be explained by the morphological re-configuration during the charge–discharge process, thus allowing the activation of additional ZnFe<sub>2</sub>O<sub>4</sub> particles in each mesoporous spheres to react with Li which were initially not reachable by lithium. For comparison, Chowdari synthesized submicrometer size ZnFe<sub>2</sub>O<sub>4</sub> using a urea combustion method, which exhibited a stable capacity of 615 mAh g<sup>-1</sup> at a specific current of 0.06 A g<sup>-1</sup> [39]; NuLi et al. synthesized the Ag-doped ZnFe<sub>2</sub>O<sub>4</sub> films and reported a reversible capacity of just 700 mAh g<sup>-1</sup> [22]; Deng prepared ZnFe<sub>2</sub>O<sub>4</sub>/C hollow spheres by a hydrothermal reaction which exhibited a specific capacity of 841 mAh g<sup>-1</sup> after 30 cycles at 0.65 A g<sup>-1</sup> [38]. Although, Ju reported a relative high capacity of 910 mAh g<sup>-1</sup> at 0.06 A g<sup>-1</sup> for ZnFe<sub>2</sub>O<sub>4</sub> after 80 cycles, they used high toxic N<sub>2</sub>H<sub>4</sub>·H<sub>2</sub>O during the synthesis [26]. Recently, Bresser et al. presented the best results in terms of high rate capability as for the synthesis of ZnFe<sub>2</sub>O<sub>4</sub>/C, showing an initial specific capacity of approximately 985 mAh g<sup>-1</sup> at the specific current of 0.02 A g<sup>-1</sup> and the capacity is increasing gradually, finally stabilizing at around 1300 mAh g<sup>-1</sup> for a specific current of 0.04 A g<sup>-1</sup> [24]. Mueller et al. investigated ZnFe<sub>2</sub>O<sub>4</sub>/C using sucrose, citric acid, and oleic acid as carbon resources respectively. ZnFe<sub>2</sub>O<sub>4</sub>/sucrose showed excellent capacity retention. An initial charge capacity of 1050 mAh g<sup>-1</sup> was obtained and it increased to around 1100 mAh g<sup>-1</sup> after 60 cycles at the specific current of 0.05 A g<sup>-1</sup> [25]. Our electrodes obviously outperformed the majority reports in capacity, cycling stability, or environmental benignity in synthesis.

Because of low electrical conductivity and large volume change of the electrode material during charge/discharge process, poor rate performance was expected for conventional micrometer-sized ZnFe<sub>2</sub>O<sub>4</sub>. The rate performance of ZnFe<sub>2</sub>O<sub>4</sub> and ZnFe<sub>2</sub>O<sub>4</sub>/C electrodes were comparatively studied by cycling at different rates between 0.1 and 1.1 A g<sup>-1</sup>. As shown in **Fig. 10b**, for the ZnFe<sub>2</sub>O<sub>4</sub>/C electrode, attractive capacities of around 1050, 920, 870 and 600 mAh g<sup>-1</sup> were achieved at specific currents of 0.1, 0.2, 0.5 and 1.0 A g<sup>-1</sup>, respectively, while the corresponding values are 780, 538, and 334 mAh g<sup>-1</sup> for the pure ZnFe<sub>2</sub>O<sub>4</sub> electrode at the specific currents of 0.1, 0.2, 0.5 A g<sup>-1</sup> (**Fig. 10c**). It suggests the as-prepared ZnFe<sub>2</sub>O<sub>4</sub>/C mesoporous microspheres may be used as electrode in power batteries. The superior rate capacity of ZnFe<sub>2</sub>O<sub>4</sub>/C to ZnFe<sub>2</sub>O<sub>4</sub>

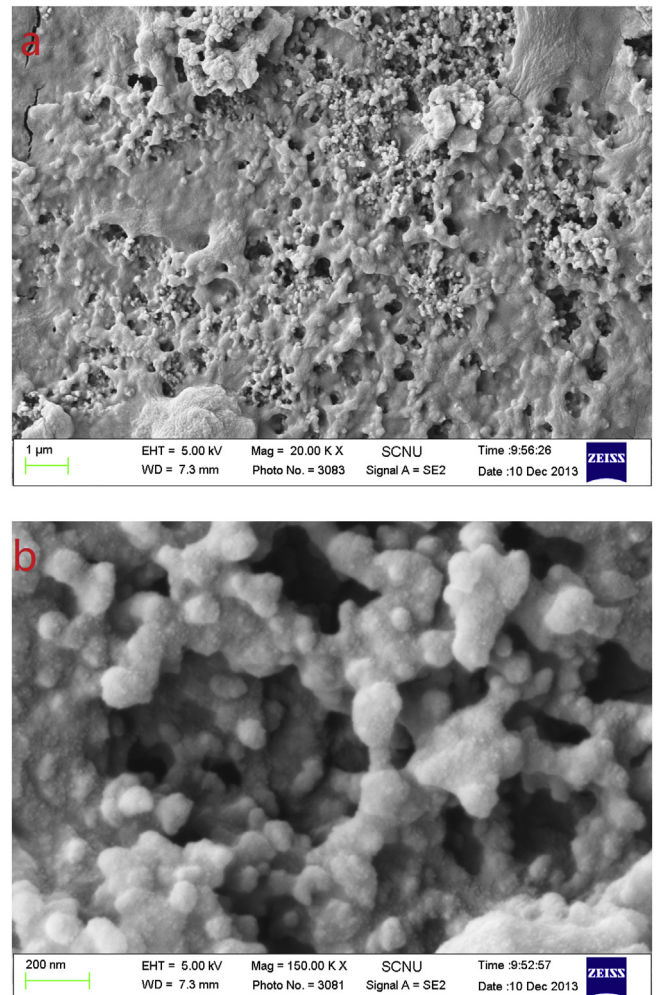


**Fig. 11.** (a and b) SEM images of ZnFe<sub>2</sub>O<sub>4</sub>/C electrodes after 100 cycles under the specific current of 0.05 A g<sup>-1</sup>.

could be assigned to the improved conductivity from carbon coating and the rich mesopores. The electrochemical performance of the ZnFe<sub>2</sub>O<sub>4</sub>/C electrode also demonstrated good stability. As shown in **Fig. 10b**, after repeated charge–discharge test at different specific currents with step increase from 0.1 to 1.1 A g<sup>-1</sup> for 50 cycles and then re-set to 0.1 A g<sup>-1</sup>, approximately 90% of initial capacity at 0.1 A g<sup>-1</sup> specific current was recovered.

SEM images of ZnFe<sub>2</sub>O<sub>4</sub>/C under the specific current of 50 mA g<sup>-1</sup> after 100 cycles have been taken. **Fig. 11a** showed that many pores appeared on the surface of the electrode, which is good to the Li<sup>+</sup> diffusion. The primary large microspheres (about 1–1.5 μm) cracked into relatively small spheres with dozens of nanometers (**Fig. 11b**). Spaces among particles could alleviate the volume expansion. Additionally, the electrode was covered by a thin film and a polymeric layer was formed on the nanoparticles surface. The behavior that the reversible capacity exceeded the theoretical specific capacity might be related to the formation of polymeric layer, the amorphous carbon and the conductive agent [24,25]. The excellent electrochemical performance of ZnFe<sub>2</sub>O<sub>4</sub>/C mesoporous microspheres can be explained as follows. Firstly, the primary nanoparticles increased the interfacial surface area for Li reaction and shortened the transport length for ions and electrons, subsequently, making the conversion reaction more flexible and then leading to a high reversible capacity; secondly, mesoporous

ZnFe<sub>2</sub>O<sub>4</sub>/C microspheres facilitated the Li<sup>+</sup> diffusion from liquid electrolyte to active electrode sites with less polarization resistance; more importantly, the mesopores and interstitial space could effectively accommodate the mechanical strains caused by the volume expansion during the charge–discharge process, thus alleviating the pulverization and improving the cycle performance; In addition, the ZnFe<sub>2</sub>O<sub>4</sub> nanoparticles embedded into the carbon network were beneficial to improve the intrinsic electrical conductivity, thus making the ZnFe<sub>2</sub>O<sub>4</sub> electrode adapt well to the rapid ion transport and a high contact area between the electrode and the electrolyte.

#### 4. Conclusion

In summary, a new facile and green way for the preparation of mesoporous ZnFe<sub>2</sub>O<sub>4</sub>/C microspheres was developed based on hydrothermal process with the presence of citric acid as an organic carbon source. The resulted materials showed outstanding performance as anodes of lithium-ion battery (LIBs) with respect to capacity, rate capability and cycling stability. ZnFe<sub>2</sub>O<sub>4</sub>/C electrode exhibited initial charge–discharge capacities of 1169 and 1551 mAh g<sup>-1</sup> with an initial coulombic efficiency of 75.5%. A specific reversible capacity of ~1100 mAh g<sup>-1</sup> after 100 cycles at the specific current of 0.05 A g<sup>-1</sup> was still obtained. Even at the specific currents of 0.2 and 1.1 A g<sup>-1</sup>, reversible capacities as high as 900 and 600 mAh g<sup>-1</sup> were still retained, respectively. The excellent cycling performance can be ascribed to the special microstructure and morphological design. The mesoporous structure with nanoparticles building blocks could accommodate the mechanism strains and provide free channels for the rapid ion transport and provide a high contact area between the electrode and the electrolyte, while the carbon coating could improve the mechanical strength as well as increase the electric contact and conductivity. As a result, the ZnFe<sub>2</sub>O<sub>4</sub>/C exhibited improved electrochemical performance. A combination of environmentally friendly synthesis, low cost and excellent electrochemical performance promises ZnFe<sub>2</sub>O<sub>4</sub>/C as an alternative anode for LIBs with a high application potential.

#### Acknowledgments

This work was financially supported by the Scientific Research and Cultivating Fund of Young Teachers in South China Normal University, the National Science Foundation of China (NSFC, Nos. 51201066 and 51171065), the Natural Science Foundation of Guangdong Province (Nos. S2012020010937, 10351063101000001), Foundation for Distinguished Young Talents in Higher Education of Guangdong (No. 2012LYM\_0048) and the Scientific Research Foundation of Graduate School of South China Normal University. The author also acknowledges ARC future fellowship.

#### References

- [1] B. Liu, P. Soares, C. Checkles, Y. Zhao, G.H. Yu, *Nano Lett.* 13 (2013) 3414–3419.
- [2] H. Li, Q. Zhao, W. Wang, H. Dong, D.S. Xu, G.J. Zou, H.L. Duan, D.P. Yu, *Nano Lett.* 13 (2013) 1271–1277.
- [3] M.V. Reddy, G.V. Subba Rao, B.V.R. Chowdari, *Chem. Rev.* 113 (2013) 5364–5457.
- [4] M.J. Osiak, E. Armstrong, T. Kennedy, C.M.S. Torres, K.M. Ryan, C. O'Dwyer, *ACS Appl. Mater. Interfaces* 5 (2013) 8195–8202.
- [5] B. Zhao, Z.P. Shao, *J. Phys. Chem. C* 116 (2012) 17440–17447.
- [6] H.G. Jung, M.W. Jang, J. Hassoun, Y.K. Sun, B. Scrosati, *Nat. Commun.* 2 (2011) 516–521.
- [7] Z.X. Yang, G.D. Du, Z.P. Guo, X.B. Yu, Z.X. Chen, T.L. Guo, H.K. Liu, *J. Mater. Chem.* 21 (2011) 8591–8596.
- [8] H.G. Wen, S.M. Cui, H.J. Kim, S. Mao, K.H. Yu, G.H. Lu, H.H. Pu, O. Mao, J.H. Chen, *J. Mater. Chem.* 22 (2012) 3300–3306.
- [9] H.S. Kim, K.Y. Chung, B.W. Cho, *J. Power Sources* 189 (2009) 108–113.
- [10] Q. Si, K. Hanai, T. Ichikawa, A. Hirano, N. Imanishi, O. Yamamoto, Y. Takeda, *J. Power Sources* 196 (2011) 6982–6986.
- [11] Zhonghui Cui, Xiangxin Guo, Hong Li, *J. Power Sources* 244 (2013) 731–735.
- [12] G.M. Zhou, D.W. Wang, F. Li, L.L. Zhang, N. Li, Z.S. Wu, L. Wen, G. Qing (Max) Lu, H.M. Cheng, *Chem. Mater.* 22 (2010) 5306–5313.
- [13] Z.Y. Wang, Z.C. Wang, S. Madhavi, X.W. (David) Lou, *J. Mater. Chem.* 22 (2012) 2526–2531.
- [14] Q.M. Zhang, Z.C. Shi, Y.F. Deng, J. Zheng, G.C. Liu, G.H. Chen, *J. Power Sources* 197 (2012) 305–309.
- [15] Q.S. Xie, F. Li, H.Z. Guo, L.S. Wang, Y.Z. Chen, G.H. Yue, D.L. Peng, *ACS Appl. Mater. Interfaces* 5 (2013) 5508–5517.
- [16] H. Liu, G.X. Wang, J. Liu, S.Z. Qiao, H.J. Ahn, *J. Mater. Chem.* 21 (2011) 3046–3052.
- [17] Y.I. Xiao, J.T. Zai, L.Q. Tao, B. Li, Q.Y. Han, C. Yu, X.F. Qian, *Phys. Chem. Chem. Phys.* 15 (2013) 3939–3945.
- [18] C.F. Zhang, H.B. Wu, Z.P. Guo, X.W. (David) Lou, *Electrochim. Commun.* 20 (2012) 7–10.
- [19] B.S. Randhawa, J. Singh, H. Kaur, M. Kaur, *Ceram. Int.* 36 (2010) 1993–1996.
- [20] Y.N. NuLi, Q.Z. Qin, *J. Power Sources* 142 (2005) 292–297.
- [21] B. Li, H. Cao, J. Shao, G. Li, M. Qu, G. Yin, *Inorg. Chem.* 50 (2011) 1628–1632.
- [22] Y. NuLi, Y.Q. Chu, Q.Z. Qin, *J. Electrochem. Soc.* 151 (2004) A1077–A1083.
- [23] M.M. Bahout, S. Bertrand, O. Pena, *J. Solid State Chem.* 178 (2005) 1080–1086.
- [24] D. Bresser, E. Paillard, R. Kloepsch, S. Krueger, M. Fiedler, R. Schmitz, D. Baither, M. Winter, S. Passerini, *Adv. Energy Mater.* 3 (2013) 513–523.
- [25] F. Mueller, D. Bresser, E. Paillard, M. Winter, S. Passerini, *J. Power Sources* 236 (2013) 87–94.
- [26] Z. Xing, Z.C. Ju, J. Yang, H.Y. Xu, Y.T. Qian, *Nano Res.* 5 (2012) 477–485.
- [27] J.H. Sui, C. Zhang, D. Hong, J. Li, Q.Z.G. Cheng, W.C. Li, *J. Mater. Chem.* 22 (2012) 13674–13681.
- [28] C.T. Cherian, M.V. Reddy, G.V. Subba Rao, C.H. Sow, B.V.R. Chowdari, *J. Solid State Electrochem.* 16 (2012) 1823–1832.
- [29] H.Y. Xu, X.L. Chen, L. Chen, L. Li, L.Q. Xu, J. Yang, Y.T. Qian, *Int. J. Electrochem. Sci.* 7 (2012) 7976–7983.
- [30] X.W. (David) Lou, L.A. Archer, Z.C. Yang, *Adv. Mater.* 20 (2008) 3987–4019.
- [31] L.M. Yao, X.H. Hou, S.J. Hu, Q. Ru, X.Q. Tang, L.Z. Zhao, D.W. Sun, *J. Solid State Electrochem.* 17 (2013) 2055–2060.
- [32] Y. Ding, Y.F. Yang, H.X. Shao, *Electrochim. Acta* 56 (2011) 9433–9438.
- [33] P.G. Bruce, B. Scrosati, J.M. Tarascon, *Angew. Chem. Int. Ed.* 47 (2008) 2930–2946.
- [34] A.S. Arico, P. Bruce, B. Scrosati, J.M. Tarascon, W.V. Schalkwijk, *Nat. Mater.* 4 (2005) 366–377.
- [35] L.M. Yao, X.H. Hou, S.J. Hu, Q. Ru, X.Q. Tang, Xiang Liu, Qiang Ru, *J. Alloys Compd.* 585 (2014) 398–403.
- [36] L.B. Chen, X.H. Xie, B.F. Wang, K. Wang, J.Y. Xie, *Mater. Sci. Eng. B* 131 (2006) 186–190.
- [37] X.W. Guo, X. Lum, X.P. Fang, Y. Mao, Z.X. Wang, L.Q. Chen, X.X. Xu, H. Yang, Y.N. Liu, *Electrochim. Commun.* 12 (2010) 847–850.
- [38] Y.F. Deng, Q. Zhang, S.D. Tang, L.T. Zhang, S.N. Deng, Z.C. Shi, G.H. Chen, *Chem. Commun.* 47 (2011) 6828–6830.
- [39] Y. Sharma, N. Sharma, G.V. SubbaRao, B.V.R. Chowdari, *Electrochim. Acta* 53 (2008) 2380–2385.
- [40] B. Zhao, X. Yu, R. Cai, R. Ran, H.T. Wang, Z.P. Shao, *J. Mater. Chem.* 22 (2012) 2900–2907.
- [41] Y.S. Yoon, S.H. Jee, S.H. Lee, S.C. Nam, *Surf. Coat. Technol.* 206 (2011) 553–558.
- [42] Z.L. Zhang, Y.H. Wang, Q.Q. Tan, Z.Y. Zhong, F.B. Su, *J. Colloid Interface Sci.* 398 (2013) 185–192.